Full length article

Steps and {11$\bar{2}$1} secondary twinning associated with {11$\bar{2}$2} twin in titanium

Mingyu Gong [a, 1], Shun Xu [a, 1], Dongyue Xie [a], Shujuan Wang [b], Jian Wang [a, c, *], Christophe Schuman [d], Jean-Sébastien Lecomte [d]

[a] Mechanical and Materials Engineering, University of Nebraska-Lincoln, Lincoln, NE 68588, USA
[b] MST-8, Los Alamos National Laboratory, Los Alamos, NM 87545, USA
[c] Nebraska Center for Materials and Nanoscience, University of Nebraska-Lincoln, Lincoln, NE 68588, USA
[d] Laboratoire d'Etude des Microstructures et de Mecanique des Materiaux (LEM3), CNRS UMR 7239, Laboratory of Excellence on Design of Alloy Metals for low-mAss Structures (DAMAS), Universite de Lorraine, F-57045, Metz, France

ABSTRACT

{11$\bar{2}$2} twinning commonly takes place in α-titanium (α-Ti). High-resolution transmission electron microscopies (HRTEM) explored various steps along {11$\bar{2}$2} coherent twin boundary. Topological model of {11$\bar{2}$2} twin revealed twinning disconnections (TDs) that are represented by (b_i, $ih_{\{11\bar{2}2\}}$) corresponding to a step height $ih_{\{11\bar{2}2\}}$ and a shear vector b_i. Atomistic simulations were conducted to study the energies and kinetics of TDs. Combining microscopies and atomistic simulations, we concluded that (b_3, $3h_{\{11\bar{2}2\}}$) is the elementary TD and (b_1, $h_{\{11\bar{2}2\}}$) is the reassembly TD. Steps observed in HRTEM thus can be treated as a reassembly of (b_3, $3h_{\{11\bar{2}2\}}$) TDs and (b_1, $h_{\{11\bar{2}2\}}$) TDs. In addition, Electron Backscatter Diffraction (EBSD) maps revealed {11$\bar{2}$2}→{11$\bar{2}$1} double twins in α-Ti. Using two-dimensional and three-dimensional atomistic simulations, we demonstrated the nucleation of (b_1, $h_{\{11\bar{2}2\}}$) TD and {11$\bar{2}$2}→{11$\bar{2}$1} double twin through the interaction between basal <a> dislocation and {11$\bar{2}$2} twin. Our results enrich the understanding of {11$\bar{2}$2} twinning including TDs, steps, and {11$\bar{2}$1} secondary twins in hexagonal metals.

© 2018 Acta Materialia Inc. Published by Elsevier Ltd. All rights reserved.

1. Introduction

Twinning is a major deformation mode in α-Ti at room temperature to accommodate strain along the c-axis of the hexagonal close packed (hcp) structure. Six twinning modes have been reported to date, including three extension twins $\left\{10\bar{1}2\right\}\left\langle\bar{1}011\right\rangle$, $\left\{11\bar{2}1\right\}\left\langle\bar{1}\bar{1}26\right\rangle$ and $\left\{11\bar{2}3\right\}\left\langle\bar{1}\bar{1}22\right\rangle$ and three compression twins $\left\{11\bar{2}2\right\}\left\langle11\bar{2}\bar{3}\right\rangle$, $\left\{10\bar{1}1\right\}\left\langle10\bar{1}\bar{2}\right\rangle$ and $\left\{11\bar{2}4\right\}\left\langle22\bar{4}\bar{3}\right\rangle$ [1,2]. Compression twins are favorable under effective compression along the c-axis or effective tension perpendicular to the c-axis.

Opposite loadings enable the activation of extension twins. $\left\{10\bar{1}2\right\}\left\langle\bar{1}011\right\rangle$ extension twins and $\left\{11\bar{2}2\right\}\left\langle11\bar{2}\bar{3}\right\rangle$ compression twins are most commonly observed in α-Ti at room temperature disregarding strain rates [3–5]. Other twinning modes have been observed while they show strong dependence on temperature, grain size and strain rate [1,6–9].

{11$\bar{2}$2} twinning is widely observed in α-Ti under compression along the normal direction of rolled sheets [10], tension along the rolling direction [11] and monotonic simple shear tests [12] by optical and electronic microscopes [13–16]. {11$\bar{2}$2} twin exhibits a lenticular shape. Moreover, {11$\bar{2}$2}→{10$\bar{1}$2} and {11$\bar{2}$2}→{11$\bar{2}$1} double twins are often observed in α-Ti [2,10]. Associated with formation of twins and double twins, twin boundaries form and act as barriers to the motion of dislocations, subsequently affecting twinning, de-twinning, and slip processes [17–19] and resulting in increased strain hardening [20,21]. However, fundamental issues of

$\{11\bar{2}2\}$ twinning, such as nucleation mechanisms and the elementary twinning disconnections (TDs), are not comprehensively understood. Nucleation of $\{11\bar{2}2\}$ twin could be complicated as $\{10\bar{1}2\}$ twinning because of its small Burges vector of the corresponding TDs and complex atomic shuffles. Recently, in situ/ex situ microscopies and atomistic simulations made a breakthrough in the nucleation of $\{10\bar{1}2\}$ twin. Pure-shuffle nucleation mechanism was demonstrated for $\{10\bar{1}2\}$ twinning [22–24]. This mechanisms is distinct from conventional understanding of either the pole-mechanisms [25] or the successive TDs-gliding mechanisms [26,27]. A comprehensive study of $\{11\bar{2}2\}$ twin nucleation is needed but exceeds the current focus of this work.

Disregarding the nucleation of $\{11\bar{2}2\}$ twins, twin propagates or grows through the shear-shuffle mechanisms via twinning disconnection [28] which is described by a dislocation $\boldsymbol{b}$ and a step of height h [29], referred to as ($\boldsymbol{b_i}$, $ih_{\{11\bar{2}2\}}$) TD. Using shear with interference method, Rapperport and Hartley [30] determined the twin shear of $\{11\bar{2}2\}$ twinning in Zr to be 0.21 ± 0.02, which agrees with the theoretical value of 0.218 associated with the shear of ($\boldsymbol{b_3}$, $3h_{\{11\bar{2}2\}}$) TD [1,31,32]. Thus, ($\boldsymbol{b_3}$, $3h_{\{11\bar{2}2\}}$) TD is accepted to be the elementary TD associated with $\{11\bar{2}2\}$ twinning. Serra et al. studied the glide of ($\boldsymbol{b_3}$, $3h_{\{11\bar{2}2\}}$) TD using molecular dynamic (MD) method and found that [33] ($\boldsymbol{b_{-1}}$, $-h_{\{11\bar{2}2\}}$) TD was emitted from the core of ($\boldsymbol{b_3}$, $3h_{\{11\bar{2}2\}}$) TD under 550 MPa shear stress at 500 K, transforming ($\boldsymbol{b_3}$, $3h_{\{11\bar{2}2\}}$) TD to ($\boldsymbol{b_4}$, $4h_{\{11\bar{2}2\}}$) TD. It must be noticed that the glide of $\boldsymbol{b_1}$ and $\boldsymbol{b_3}$ on the twin plane results in the opposite shear, corresponding to compression or tension twinning. From the point of crystallographic view, the resulted twin structures are identical although the shear deformation gradient is opposite. In other words, $\{11\bar{2}2\}$ twinning is of extension if the twin shear is associated with $\boldsymbol{b_1}$, or of compression as the twin shear is associated with $\boldsymbol{b_3}$. This raises fundamental issues: does the ($\boldsymbol{b_1}$, $h_{\{11\bar{2}2\}}$) TD exist on the coherent twin boundary? Why isn't ($\boldsymbol{b_1}$, $h_{\{11\bar{2}2\}}$) the elementary TD? For other TDs ($\boldsymbol{b_2}$, $2h_{\{11\bar{2}2\}}$), ($\boldsymbol{b_4}$, $4h_{\{11\bar{2}2\}}$), ($\boldsymbol{b_5}$, $5h_{\{11\bar{2}2\}}$), ($\boldsymbol{b_6}$, $6h_{\{11\bar{2}2\}}$) and ($\boldsymbol{b_7}$, $7h_{\{11\bar{2}2\}}$), how do they form during twinning?

Accompanying with twin propagation, twin boundaries act as barriers to the motion of dislocations, affecting consequent deformation modes, such as the migration of twin boundary accompanied with the formation of TDs or steps [34–36], secondary twinning [37,38] and slip transformation [39–41]. Using MD simulation, Serra et al. [35] found that basal $<\boldsymbol{a}>$ dislocations are blocked by the $\{11\bar{2}2\}$ coherent twin boundary (CTB). Capolungo et al. [42] compared the stress-strain curves of the samples with/out pre-existing $\{11\bar{2}2\}$ twins, and found a softer response for the sample containing pre-existing $\{11\bar{2}2\}$ twins and the easy activation of prismatic dislocations in the twin. Salem et al. [43] found that $\{11\bar{2}2\}$ twins are always harder than matrix based on micro- and nano-hardness measurements in Ti and ascribed the hardening to the trapping of sessile dislocations in the twin. Xu et al. [2] proposed the nucleation of $\{11\bar{2}2\} \rightarrow \{11\bar{2}1\}$ double twins through the interaction between basal $<\boldsymbol{a}>$ dislocation and $\{11\bar{2}2\}$ CTB. Atomistic simulations have been widely employed to explore the interactions between dislocations and twin boundaries [34–36,40]. Recently, Gong et al. [44] reported on the formation of steps/facets, the cross-slip of dislocations, and the creation of stacking faults in Mg alloys as basal dislocations interact with three-dimensional $\{10\bar{1}2\}$ twins. Here, we studied the interactions between basal $<\boldsymbol{a}>$ dislocations and $\{11\bar{2}2\}$ twin to address the formation of steps

and $\{11\bar{2}1\}$ secondary twin.

This work aims to provide comprehensive understanding of TDs, steps and secondary twinning associated with $\{11\bar{2}2\}$ twins through combining microscopes with atomistic simulations. This article is organized as follows. In section 2, we reported on experimental observations of $\{11\bar{2}2\}$ twins, including $\{11\bar{2}2\} \rightarrow \{11\bar{2}1\}$ double twins based on Electron Backscatter Diffraction (EBSD) maps and steps along $\{11\bar{2}2\}$ CTB according to high-resolution transmission electron microscopies (HRTEM). In section 3, we briefly reviewed characters of ($\boldsymbol{b_i}$, $ih_{\{11\bar{2}2\}}$) TDs based on topological model of $\{11\bar{2}2\}$ twin. Furthermore, we conducted molecular statics (MS) and molecular dynamics (MD) simulations of TDs in terms of their energies and kinetics. In section 4, we performed two-dimensional and three-dimensional MD simulations of the $<\boldsymbol{a}>$ dislocations - $\{11\bar{2}2\}$ twin interactions. Finally, we draw conclusions based on microscopes and atomistic simulations.

2. Experimental observations of $\left\{11\bar{2}2\right\}$ twins

The rolled commercially pure titanium T40 sheet (ASTM grade 2) with the thickness of 1.5 mm was annealed in a vacuum furnace at 800 °C for 3 h. Using a Zwick 120T machine, the annealed sheet was subjected to a compressive strain of 5.1% at a strain rate $1.0 \times ^{-3} s^{-1}$ at room temperature. The compression direction is along the normal direction of the sheet. After that, the surface of the deformed sample was ground with SiC papers of grits from 1200# to 4000#. Electrolytic polishing was performed in a solution of 10% perchloric acid and 90% methanol at 35 V for 5 s at 5 °C. EBSD measurements were applied on a JEOL JSM-6500F field emission gun scanning electron microscopy (SEM) equipped with an EBSD camera and the AZtec acquisition software package (Oxford Instruments).

2.1. Morphology of $\left\{11\bar{2}2\right\}$ twins

We detected 68 $\{11\bar{2}2\}$ deformation twins and 4 $\{\bar{1}012\}$ deformation twins in the area of 0.15 mm^2 by using EBSD, showing $\{11\bar{2}2\}$ twinning is dominate under current loading. All of the $\{11\bar{2}2\}$ twins have regular lenticular shape disregarding observed directions. A typical EBSD map is shown in Fig. 1a. In grain A, two $\{11\bar{2}2\}$ twins are labeled by the red and yellow squares, respectively. For twin B, the pole figures of $\left\langle 10\bar{1}0 \right\rangle$ and $\left\langle 11\bar{2}3 \right\rangle$ directions in the parent grain and the twin are depicted in Fig. 1b and c. It can be noticed in Fig. 1b that the $\left\langle 10\bar{1}0 \right\rangle$ zone direction (ZD) is closely oriented to the center of the pole figure, which represents the observation direction (OD). The twinning shear direction is near the edge of the pole figure in Fig. 1c. For twin C, the zone direction is largely deviated from the OD as shown in Fig. 1d and the twining shear direction as shown in Fig. 1e. In both cases, twins exhibit a lenticular shape.

2.2. Steps along $\left\{11\bar{2}2\right\}$ CTB

We characterized steps along $\{11\bar{2}2\}$ CTB. Fig. 2a shows a twin band taken along the $[1\bar{1}00]$ zone axis. The selected area electron diffraction (SAED) pattern confirms that the band is of $\{11\bar{2}2\}$ twin. Fig. 2b shows multiple steps with the step heights in the order of 2:4:3. Fig. 2c shows multiple steps with the step heights in the order of 3:3:2:3:4. Fig. 2d shows multiple steps with the step heights in the order of 7:2:5:2:2. It is noticed that each step isn't always equal to $3nh_{\{11\bar{2}2\}}$ ($n \geq 1$). However, it's interesting that the
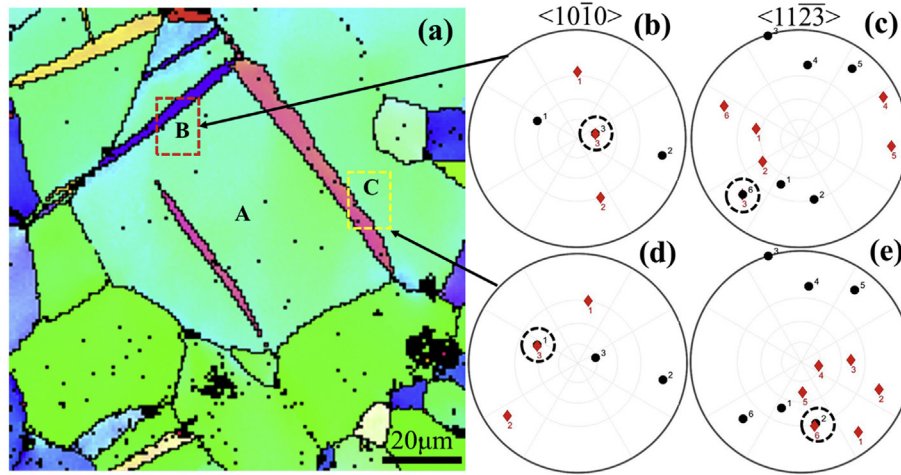
Fig. 1. (a) A typical EBSD map of the sample that is subjected to a compressive strain of 5.1%. The pole figures of (b) $\langle 10\bar{1}0 \rangle$ and (c) $\langle 11\bar{2}3 \rangle$ direction for twin B as marked in (a). The pole figures of (d) $\langle 10\bar{1}0 \rangle$ and (e) $\langle 11\bar{2}3 \rangle$ direction for twin C as marked in (a). The view direction is located in the center of the pole figures. In all pole figures, black dots and red diamonds represent the directions in the parent grain and primary twin, respectively. (For interpretation of the references to color in this figure legend, the reader is referred to the Web version of this article.)
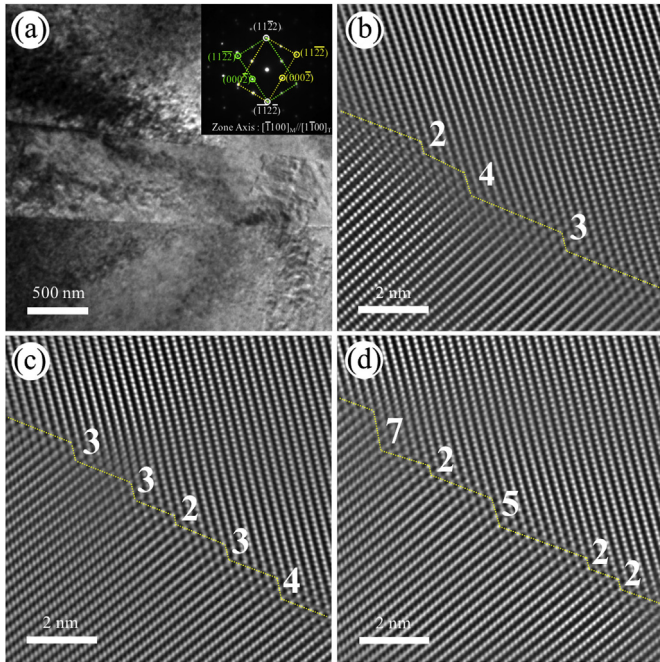

Fig. 2. (a) The bright field TEM image of the $\{11\bar{2}2\}$ twin. The inserted SAED pattern confirms twin orientation. (b)–(d) HAADF images of twin boundary, showing multiple Steps.

total height of these steps shown in Fig. 2b−d are equal to $3nh_{\{11\bar{2}2\}}$ ($n \geq 1$), i.e., $9h_{\{11\bar{2}2\}}$, $15h_{\{11\bar{2}2\}}$ and $18h_{\{11\bar{2}2\}}$, respectively. This feature is generally true in other 7 HRTEM images. Therefore, ($\boldsymbol{b_3}$, $3h_{\{11\bar{2}2\}}$) TD might be the elementary TD associated with $\{11\bar{2}2\}$ twinning. Non-$3nh_{\{11\bar{2}2\}}$ steps can be treated as reassembled steps associated with nucleation and reassembly of ($\boldsymbol{b_1}$, $h_{\{11\bar{2}2\}}$) TD. For example, the steps (2:4:3) in Fig. 2b form through the following reactions. The 2-layer step is due to the dissociation of ($\boldsymbol{b_3}$, $3h_{\{11\bar{2}2\}}$) TD into ($\boldsymbol{b_2}$, $2h_{\{11\bar{2}2\}}$) + ($\boldsymbol{b_1}$, $h_{\{11\bar{2}2\}}$) TDs, the dissociated ($\boldsymbol{b_1}$, $h_{\{11\bar{2}2\}}$) reacts with the other ($\boldsymbol{b_3}$, $3h_{\{11\bar{2}2\}}$) to form ($\boldsymbol{b_4}$, $4h_{\{11\bar{2}2\}}$), i.e., one 4-

layer step. Thus the 2:4:3 steps are a result of dissociation and reassembly of the 3:3:3 steps. It is reasonably believed that ($\boldsymbol{b_3}$, $3h_{\{11\bar{2}2\}}$) TD is the elementary TD associated with $\{11\bar{2}2\}$ twinning, and ($\boldsymbol{b_1}$, $h_{\{11\bar{2}2\}}$) TD is a reassembly TD associated with $\{11\bar{2}2\}$ twinning. We will further examine this thought in terms of the energetics and kinetics of steps using atomistic simulations.

2.3. $\{11\bar{2}2\} \rightarrow \{11\bar{2}1\}$ *double twin*

An EBSD map in Fig. 3a shows one $\{11\bar{2}1\}$ secondary twin inside one $\{11\bar{2}2\}$ primary twin, referred to as $\{11\bar{2}2\} \rightarrow \{11\bar{2}1\}$ double twin (a schematic in Fig. 3b). The twin modes are identified according to Fig. 3c, where point-to-point misorientation of the blue arrow labeled in Fig. 3a is presented. The misorientation angle at points A and D is around 64°, while that at points B and C is about 35°. This indicates that the double twin in Fig. 3a is $\{11\bar{2}2\} \rightarrow \{11\bar{2}1\}$. Both the primary and secondary twinning systems share the zone axis along the same $\langle 10\bar{1}0 \rangle$ direction. The pole figure of $\langle 10\bar{1}0 \rangle$ directions in Fig. 3d shows that the primary and secondary twin have the same zone axis as marked by a dashed black square, revealing that the double twin belongs to co-zone double twin. Recently, Beyerlein et al. [37] and Xu et al. [2] proposed that nucleation of secondary twin in a primary twin could be related to the interaction between glide dislocations and twin boundary. In the following section, we will test this proposal using MD simulations.

3. Twinning disconnections

3.1. Topological analysis

Using the dichromatic complex of $\{11\bar{2}2\}$ twin, we show possible shears associated with $\{11\bar{2}2\}$ twinning. Fig. 4a shows a unit cell of hexagonal close packed structure. Atoms in the unit cell are symbolized with four types (solid circle, solid triangle, open circle and open triangle) with respect to the coordinate along the $[\bar{1}100]$ direction. Circles and triangles represent atoms on A-type and B-type (0001) planes, respectively. Fig. 4b shows the
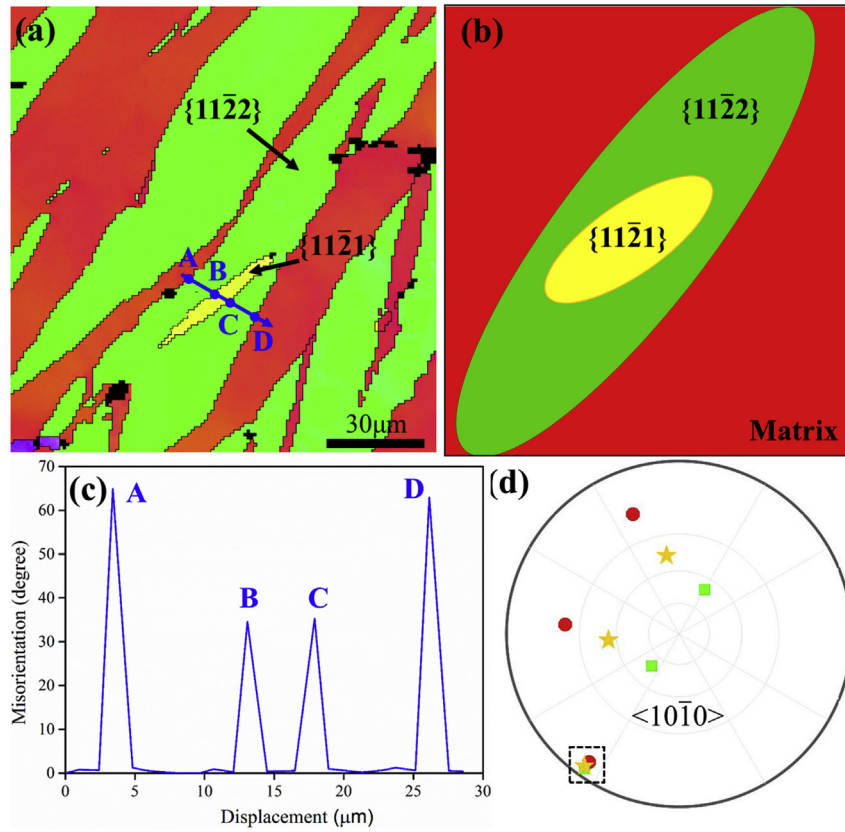
Fig. 3. (a) An EBSD map of $\{11\bar{2}2\} \rightarrow \{11\bar{2}1\}$ double twins. (b) A schematic of $\{11\bar{2}2\} \rightarrow \{11\bar{2}1\}$ double twin in (a). (c) Point-to-point misorientation along the blue arrow in (a). (d) Pole figure of $\langle 10\bar{1}0 \rangle$ zone direction of the $\{11\bar{2}2\}$ primary twin and $\{11\bar{2}1\}$ secondary twin. The red dots, green squares and yellow stars represent $\langle 10\bar{1}0 \rangle$ directions in the matrix, the primary twin and the secondary twin, respectively. (For interpretation of the references to color in this figure legend, the reader is referred to the Web version of this article.)

dichromatic complex of $\{11\bar{2}2\}$ twin. The coordinates are the x-axis along $[\bar{1}123]$ direction, the y-axis normal to $(11\bar{2}2)$ plane and the z-axis along $[\bar{1}100]$ direction. Black atoms belong to the matrix and red atoms belong to the twin. The horizontal dashed line represents the CTB. Corresponding to the upward migration of the twin boundary, black atoms will move to red atoms through shear and shuffle. Burgers vector $\boldsymbol{b_i}$ describes the direction and magnitude of the shear associated with the ith-layer transformation. The displacements of the other black atoms below the ith $(11\bar{2}2)$ plane are defined as the shuffle vectors.

Taking $(\boldsymbol{b_1}, h_{\{11\bar{2}2\}})$ TD as an example, a single-layer TD $(\boldsymbol{b_1}, h_{\{11\bar{2}2\}})$ glides on the plane between the 0th and 1st atomic planes, resulting in the one-layer upward migration of the twin boundary. The Burgers vector $\boldsymbol{b_1}$ and the resulted twin shear are

$$\boldsymbol{b_1} = \frac{a^2}{3(a^2+c^2)}\left[\bar{1}123\right], \quad S_1 = \frac{|\boldsymbol{b_1}|}{d_{(11\bar{2}2)}} = \frac{2a}{c} \tag{1}$$

for α-Ti $a = 0.295$ nm and $c = 0.468$ nm, the magnitude of $\boldsymbol{b_1}$ is 0.157 nm, the direction of $\boldsymbol{b_1}$ is along $[\bar{1}123]$ and the twin shear S_1 is equal to 1.261. This shear process doesn't involve atoms shuffling. For $(\boldsymbol{b_2}, 2h_{\{11\bar{2}2\}})$ TD, the Burgers vector $\boldsymbol{b_2}$ and the twin shear are

$$\boldsymbol{b_2} = \frac{c^2 - a^2}{3(a^2+c^2)}\left[11\bar{2}3\right], \quad S_2 = \frac{|\boldsymbol{b_2}|}{2d_{(11\bar{2}2)}} = \frac{c^2 - a^2}{ac} \tag{2}$$

The magnitude of $\boldsymbol{b_2}$ is 0.239 nm for α-Ti and the shear direction

of $\boldsymbol{b_2}$ is opposite to that of $\boldsymbol{b_1}$. Twin shear S_2 is 0.956. Fig. 4c shows shuffle vectors $\boldsymbol{s'_1}$ and $\boldsymbol{s''_1}$ for atoms on the 1st atomic plane.

$$\boldsymbol{s'_1} = \frac{c^2 - a^2}{6(a^2+c^2)}\left[11\bar{2}3\right] - \frac{1}{6}\left[1\bar{1}00\right] \tag{3}$$

$$\boldsymbol{s''_1} = \frac{c^2 - a^2}{6(a^2+c^2)}\left[11\bar{2}3\right] + \frac{1}{6}\left[1\bar{1}00\right] \tag{4}$$

The magnitudes of $\boldsymbol{s'_1}$ and $\boldsymbol{s''_1}$ are 0.147 nm for α-Ti. Using the same method, Burgers vector $\boldsymbol{b_i}$ in Fig. 4b, shear strain S_i and shuffle vectors on each plane in Fig. 4c–f are summarized in Table 1. These values are further confirmed by the MD results regarding to atom movements during glide of TDs in Supplementary figures S-2.

Corresponding to the well-accepted twin shear direction $[11\bar{2}3]$, the gliding of $\boldsymbol{b_2}$ and $\boldsymbol{b_3}$ will cause the same signed shear as the twin shear while the gliding of $\boldsymbol{b_1}$, $\boldsymbol{b_4}$ and $\boldsymbol{b_5}$ will cause the opposite signed shear to the twin shear. $\boldsymbol{b_6}$ can be treated as two $\boldsymbol{b_3}$. $\boldsymbol{b_7}$ is a near zero shear and thus can be considered as a pure step [45]. $(\boldsymbol{b_1}, h_{\{11\bar{2}2\}})$ TD might have higher mobility than others because the gliding of $(\boldsymbol{b_1}, h_{\{11\bar{2}2\}})$ TD doesn't involve atoms shuffling. The magnitude of $(\boldsymbol{b_4}, 4h_{\{11\bar{2}2\}})$ TD and corresponding twin shear S_4 are smaller than that of $(\boldsymbol{b_3}, 3h_{\{11\bar{2}2\}})$ TD. However, neither $(\boldsymbol{b_1}, h_{\{11\bar{2}2\}})$ nor $(\boldsymbol{b_4}, 4h_{\{11\bar{2}2\}})$ TD was considered to be the elementary TD associated with $\{11\bar{2}2\}$ twinning, because they don't result in the same twin shear as identified in experiments. Taking $\boldsymbol{b_3}$ as the
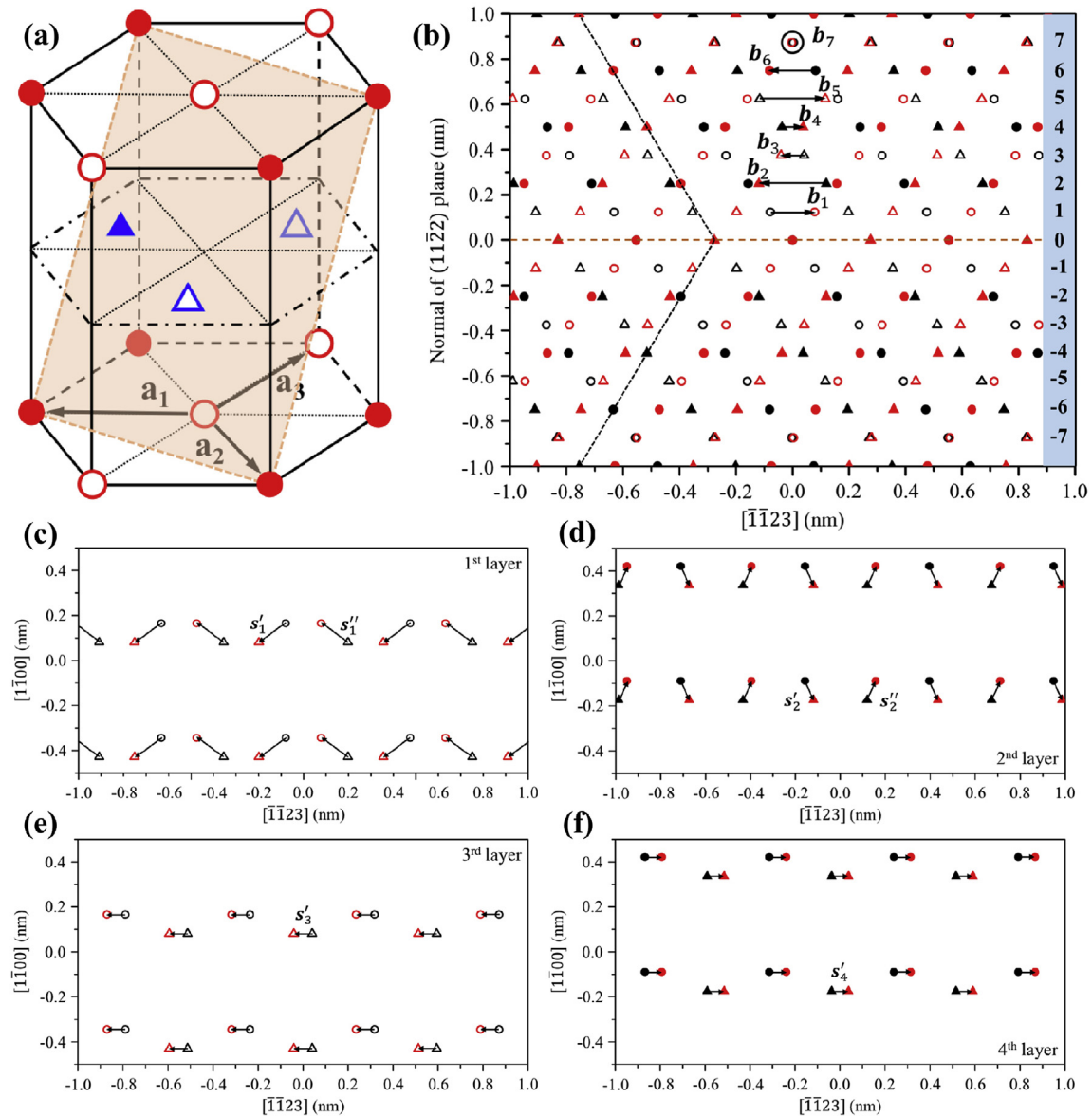
Fig. 4. (a) A hexagonal close packed (hcp) unit cell containing four types of atoms with respect to the coordinate along $[\bar{1}100]$ direction. The orange plane shows the $(11\bar{2}2)$ plane in the unit cell. (b) Dichromatic complex of $\{11\bar{2}2\}$ twin. Black atoms belong to the matrix and red atoms belong to the twin. Burgers vectors of b_1, b_2, b_3, b_4, b_5, b_6 and b_7 are defined in the dichromatic complex. Shuffle vectors of atoms in (c) 1st layer; (d) 2nd layer; (e) 3rd layer and (f) 4th layer associated with various TDs. (For interpretation of the references to color in this figure legend, the reader is referred to the Web version of this article.)

Table 1
Burgers vector b_i, shear strain S_i and shuffle vectors in α-Ti.

i	1	2	3	4	5	7
b_i /$[\bar{1}\bar{1}23]$	$\dfrac{a^2}{3(a^2+c^2)}$	$\dfrac{a^2-c^2}{3(a^2+c^2)}$	$\dfrac{2a^2-c^2}{3(a^2+c^2)}$	$\dfrac{3a^2-c^2}{3(a^2+c^2)}$	$\dfrac{4a^2-c^2}{3(a^2+c^2)}$	$\dfrac{5a^2-2c^2}{3(a^2+c^2)}$
$Sign(b_i)|b_i|$ (α-Ti)/nm	0.157	−0.239	−0.082	0.075	0.232	−0.007
S_i	$\dfrac{2a}{c}$	$\dfrac{a^2-c^2}{ac}$	$\dfrac{4a^2-2c^2}{3ac}$	$\dfrac{3a^2-c^2}{2ac}$	$\dfrac{8a^2-2c^2}{5ac}$	$\dfrac{10a^2-4c^2}{7ac}$
S_i (α-Ti)	1.261	−0.956	−0.217	0.152	0.374	−0.001

Shuffle vectors in α-Ti.

	/$[\bar{1}\bar{1}23]$	/$[1\bar{1}00]$	$|s_i|$ (nm)	Involved in		/$[\bar{1}\bar{1}23]$	/$[1\bar{1}00]$	$|s_i|$ (nm)	Involved in
s_1'	$\dfrac{a^2-c^2}{6(a^2+c^2)}$	$-\dfrac{1}{6}$	0.147	b_2, b_3, b_4, b_5	s_2''	$\dfrac{3a^2-c^2}{6(a^2+c^2)}$	$\dfrac{1}{6}$	0.038	b_3, b_4, b_5
s_1''	$\dfrac{a^2-c^2}{6(a^2+c^2)}$	$\dfrac{1}{6}$	0.147	b_2, b_3, b_4, b_5	s_3'	$\dfrac{2a^2-c^2}{3(a^2+c^2)}$	0	0.082	b_4, b_5
s_2'	$\dfrac{3a^2-c^2}{6(a^2+c^2)}$	$-\dfrac{1}{6}$	0.038	b_3, b_4, b_5	s_4'	$\dfrac{3a^2-c^2}{3(a^2+c^2)}$	0	0.075	b_5

elementary TD and $\boldsymbol{b_1}$ as a reassembly TD, these shear vectors can be related to each other, such as $\boldsymbol{b_2} = \boldsymbol{b_3} - \boldsymbol{b_1}$, $\boldsymbol{b_4} = \boldsymbol{b_3} + \boldsymbol{b_1}$ and $\boldsymbol{b_5} = 2\boldsymbol{b_3} - \boldsymbol{b_1}$. In the following, we will examine this proposal by atomistic simulations.

3.2. Energies and kinetics of TDs

Atomistic simulations were conducted to study the energies and kinetics of TDs with the embedded atom method (EAM) potential for Ti developed by Zope and Mishin [46]. The potential has been examined to reproduce fundamental properties of Ti by comparing with DFT (GGA) calculations and experimental measurements, as summarized in supplementary Table S-1. A bi-crystal corresponding to ($11\bar{2}2$) twin orientation has the dimensions of $80 \times 80 \times 1.53$ nm. The matrix adopts the coordinates: the x-axis along $[\bar{1}1\bar{2}3]$ direction, the y-axis normal to ($11\bar{2}2$) plane and the z-axis along $[\bar{1}100]$ direction. Periodic boundary conditions are applied in the x- and z-directions. Twin boundary is the x-z plane in the middle of the model. Two 1 nm thick regions in y-direction are fixed to mimic bulk property of Ti. The bi-crystal is relaxed until the force acting on each atom is less than 5 pN. To study the energy of TDs, we introduced TDs in the bi-crystal by applying the anisotropic Barnett-Lothe solutions [47] for the displacement field of a dislocation in the bi-crystal and displacing atoms according to their shuffle vectors (Table 1). We apply fixed boundary in the x- and y-direction to eliminate image force. Dislocated structures are then relaxed until the force acting on each atom is less than 5 pN. Fig. 5 shows atomic structures of six TDs. Atoms are colored according to their excess energy.

The line energy associated with each TD is computed by integrating the excess energy of each atom around the center of the dislocation core within a radius r (Å). Fig. 6a shows the line energies of five TDs with respect to $\text{Ln}(r)$. According to theory of dislocation [25], the slope of the linear part is proportional to the square of the magnitude of Burgers vector of each TD. Therefore, $\boldsymbol{b_2}$ and $\boldsymbol{b_5}$ have larger elastic energy because of their large magnitudes of 0.239 and 0.232 nm. $\boldsymbol{b_3}$ and $\boldsymbol{b_4}$ have smaller elastic energy associated with their small magnitudes of 0.082 and 0.075 nm. The magnitude of Burgers vector $\boldsymbol{b_1}$ is equal to 0.157 nm, correspondingly, the elastic

energy associated with $\boldsymbol{b_1}$ is four times larger than that of $\boldsymbol{b_3}$ and $\boldsymbol{b_4}$. The non-linear part represents the contribution of the core energy (or step energy) to the total energy of a dislocation. Corresponding to the general formula $E = E_{core}(\rho) + E_{line}(r - \rho)$, in which ρ is the dimension of the dislocation core, we determined the core energy and the core radius for $\boldsymbol{b_1}$ to $\boldsymbol{b_5}$, 0.71 eV/nm and 0.83 nm, 3.43 eV/nm and 1.38 nm, 1.75 eV/nm and 0.45 nm, 2.60 eV/nm and 0.78 nm, and 6.32 eV/nm and 3.27 nm, respectively. The results show that the nucleation of ($\boldsymbol{b_3}$, $3h_{\{11\bar{2}2\}}$) TD is energetically favored because of the lowest energy among the five TDs.

We further computed kinetic barriers associated with the glide of each TD by using Nudge Elastic Band (NEB) method with 19 intermediate states [48]. The NEB calculations are converged until the difference in the total energy within 10 iterative steps is less than 10^{-3} eV. Fig. 6b and c show the kinetic barrier corresponding to the glide of each TD. Configurations of initial, final and three intermediate states are shown in the Supplementary Table S-3. The shuffle displacements observed in atomistic simulations are consistent with topological analysis. Kinetic barrier of ($\boldsymbol{b_2}$, $2h_{\{11\bar{2}2\}}$) TD is around 100 times larger than that of ($\boldsymbol{b_1}$, $h_{\{11\bar{2}2\}}$) TD. Kinetic barriers of ($\boldsymbol{b_3}$, $3h_{\{11\bar{2}2\}}$) TD, ($\boldsymbol{b_4}$, $4h_{\{11\bar{2}2\}}$) TD and ($\boldsymbol{b_5}$, $5h_{\{11\bar{2}2\}}$) TD are around 100 times larger than that of ($\boldsymbol{b_2}$, $2h_{\{11\bar{2}2\}}$) TD. Between two ($\boldsymbol{b_3}$, $3h_{\{11\bar{2}2\}}$) TD and ($\boldsymbol{b_4}$, $4h_{\{11\bar{2}2\}}$) TD with low linear energy, ($\boldsymbol{b_3}$, $3h_{\{11\bar{2}2\}}$) TD has lower kinetic barrier, indicating the higher mobility than ($\boldsymbol{b_4}$, $4h_{\{11\bar{2}2\}}$) TD. In conclusion, ($\boldsymbol{b_3}$, $3h_{\{11\bar{2}2\}}$) TD has the lowest linear energy and relatively high mobility, which accounts for why ($\boldsymbol{b_3}$, $3h_{\{11\bar{2}2\}}$) TD is the elementary TD associated with $\{11\bar{2}2\}$ twinning. ($\boldsymbol{b_1}$, $h_{\{11\bar{2}2\}}$) TD has the lowest kinetic barrier because of the planar extended core, indicating the highest mobility.

3.3. Steps reassembly

It is noted that the line energy of a ($\boldsymbol{b_1}$, $h_{\{11\bar{2}2\}}$) TD within a radius smaller than 5.46 nm is lower than that of other TDs (Fig. 6). Taking the high mobility of ($\boldsymbol{b_1}$, $h_{\{11\bar{2}2\}}$) TD into account, a ($\boldsymbol{b_1}$,
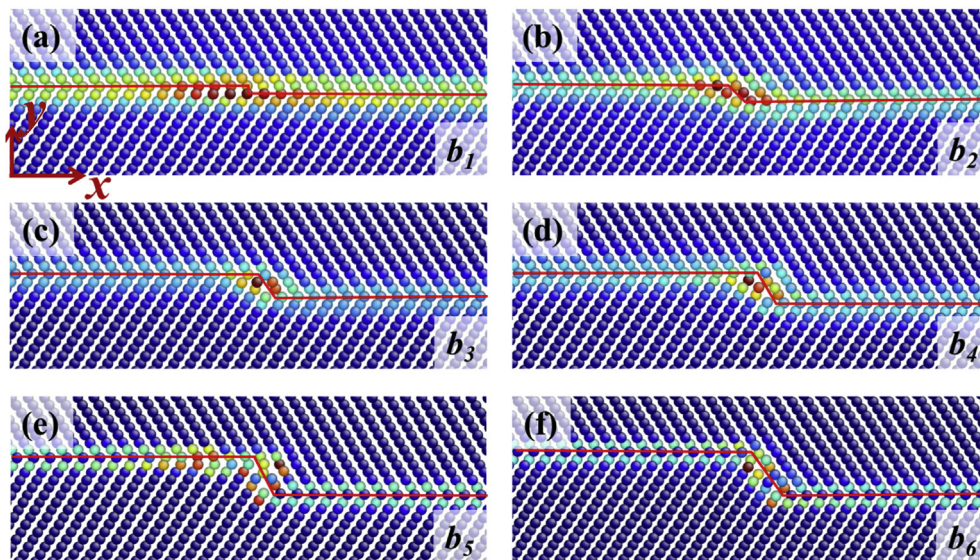

Fig. 5. Atomic structures of (a) ($\boldsymbol{b_1}$, $h_{\{11\bar{2}2\}}$) TD; (b) ($\boldsymbol{b_2}$, $2h_{\{11\bar{2}2\}}$) TD; (c) ($\boldsymbol{b_3}$, $3h_{\{11\bar{2}2\}}$) TD; (d) ($\boldsymbol{b_4}$, $4h_{\{11\bar{2}2\}}$) TD; (e) ($\boldsymbol{b_5}$, $5h_{\{11\bar{2}2\}}$) TD and (f) two ($\boldsymbol{b_3}$, $3h_{\{11\bar{2}2\}}$) TDs on the ($11\bar{2}2$) CTB. The x-axis is along $[\bar{1}1\bar{2}3]$ direction, the y-axis is normal to ($11\bar{2}2$) plane and the z-axis is along $[\bar{1}100]$ direction.
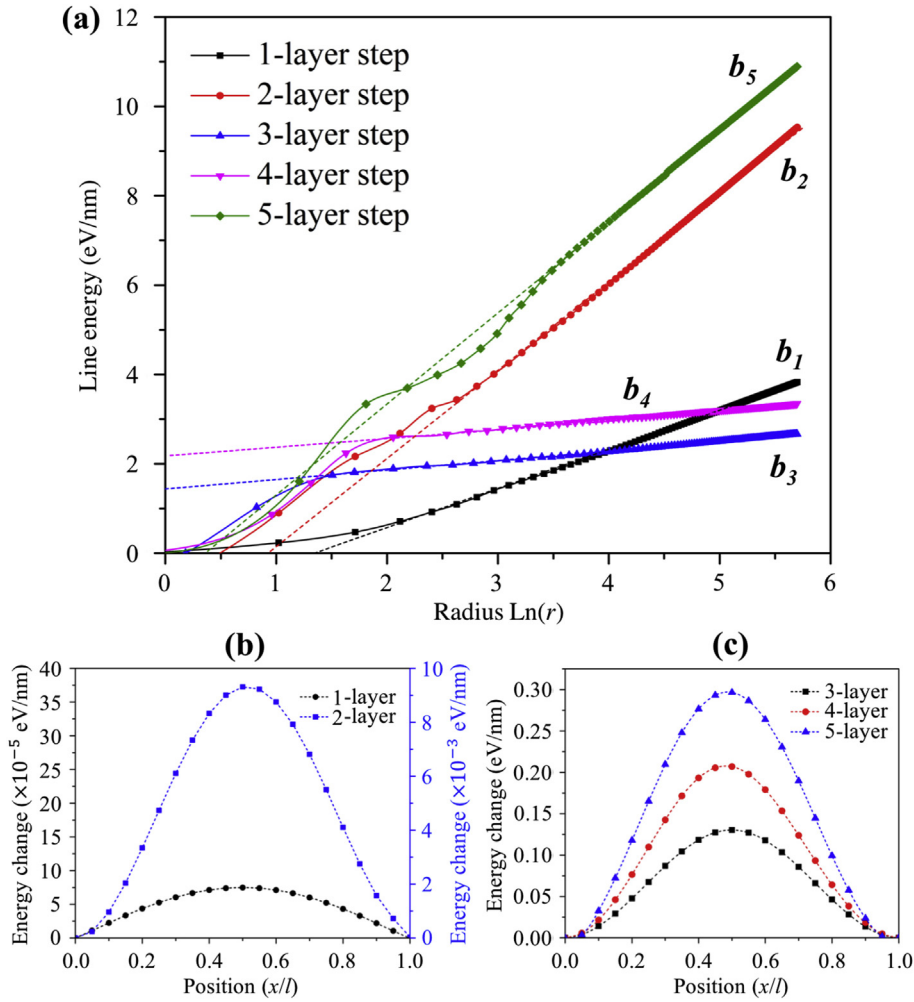
Fig. 6. Line energy associated with ($\boldsymbol{b_1}$, $h_{\{11\bar{2}2\}}$) TD, ($\boldsymbol{b_2}$, $2h_{\{11\bar{2}2\}}$) TD, ($\boldsymbol{b_3}$, $3h_{\{11\bar{2}2\}}$) TD, ($\boldsymbol{b_4}$, $4h_{\{11\bar{2}2\}}$) TD and ($\boldsymbol{b_5}$, $5h_{\{11\bar{2}2\}}$) TD with respect to Ln(r). The slopes of the linear part are in agreement with the square of the magnitude of Burgers vectors. The nonlinear part shows the dislocation core energy (or step energy). The change in potential energy associated with the glide of (a) ($\boldsymbol{b_1}$, $h_{\{11\bar{2}2\}}$) TD and ($\boldsymbol{b_2}$, $2h_{\{11\bar{2}2\}}$) TD and (b) ($\boldsymbol{b_3}$, $3h_{\{11\bar{2}2\}}$) TD, ($\boldsymbol{b_4}$, $4h_{\{11\bar{2}2\}}$) TD and ($\boldsymbol{b_5}$, $5h_{\{11\bar{2}2\}}$) TD.

$h_{\{11\bar{2}2\}}$) TD dipole could be nucleated between two ($\boldsymbol{b_3}$, $3h_{\{11\bar{2}2\}}$) TDs, i.e., two ($\boldsymbol{b_3}$, $3h_{\{11\bar{2}2\}}$) TDs (or two 3-layer steps) are reassembled, forming one ($\boldsymbol{b_2}$, $2h_{\{11\bar{2}2\}}$) TD and one ($\boldsymbol{b_4}$, $4h_{\{11\bar{2}2\}}$) TD (or one 2-layer step and one 4-layer step). Therefore, we refer ($\boldsymbol{b_1}$, $h_{\{11\bar{2}2\}}$) TD to the reassembly TD. This could explain the formation of 2-layer and 4-layer steps that are observed in HRTEM images.

Using MD simulation, we observed the nucleation of a ($\boldsymbol{b_1}$, $h_{\{11\bar{2}2\}}$) TD dipole at a three-layer step (or ($\boldsymbol{b_3}$, $3h_{\{11\bar{2}2\}}$) TD) (the same model as shown in Fig. 5c), resulting in the formation of one 4-layer step (($\boldsymbol{b_4}$, $4h_{\{11\bar{2}2\}}$) TD) and one 1-layer step (($\boldsymbol{b_1}$, $h_{\{11\bar{2}2\}}$) TD). When a three-layer step (or ($\boldsymbol{b_3}$, $3h_{\{11\bar{2}2\}}$) TD) is gliding on $\{11\bar{2}2\}$ CTB under applied shear stress $\tau_{yx} = -600$ MPa at 50 K (Fig. 7a), we observed the emission of one ($\boldsymbol{b_{-1}}$, $-h_{\{11\bar{2}2\}}$) TD from the lower corner of the three-layer step as shown in Fig. 7b. This is consistent with Serra's observation [33]. ($\boldsymbol{b_1}$, $h_{\{11\bar{2}2\}}$) TD quickly moves, detwinning the twin by one layer. Fig. 7c shows a four-layer step.

The possibility of forming steps via the pileup of ($\boldsymbol{b_1}$, $h_{\{11\bar{2}2\}}$) TDs is ruled out because of the strong repulsion among ($\boldsymbol{b_1}$, $h_{\{11\bar{2}2\}}$) TDs. We created a four-layer step by piling up four ($\boldsymbol{b_1}$, $h_{\{11\bar{2}2\}}$) TDs. MD

simulation demonstrated the dissociation of such a 4-layer step into four discrete ($\boldsymbol{b_1}$, $h_{\{11\bar{2}2\}}$) TDs, as shown in Fig. 7d.

4. Dislocation-$\left\{11\bar{2}2\right\}$ twin interactions

The dislocation-twin interaction depends strongly on the slip systems available in the twin, atomic structure of the twin boundary, the local stress state, and temperature [39,49–52]. The last two factors can be varied with loading conditions, but the first two factors are determined by the geometrical characteristics of the boundary [53]. Here, we conducted atomistic simulations at 10 K to study the interactions between a basal <$\boldsymbol{a}$> dislocation and one $\{11\bar{2}2\}$ twin.

4.1. Basal <a> dislocation interactions with a 2D $\left\{11\bar{2}2\right\}$ twin

We adopted a bi-crystal model corresponding to (11$\bar{2}$2) twin orientation. The model has the dimensions of $40 \times 40 \times 1.53$ nm. The matrix adopts the coordinates where the x-axis is along [$\bar{1}\bar{1}23$] direction, the y-axis is normal to (11$\bar{2}$2) plane and the z-axis is along [$\bar{1}100$] direction. Twin boundary is the x-z plane in the middle of the model. To study the interactions, we introduced a pure edge
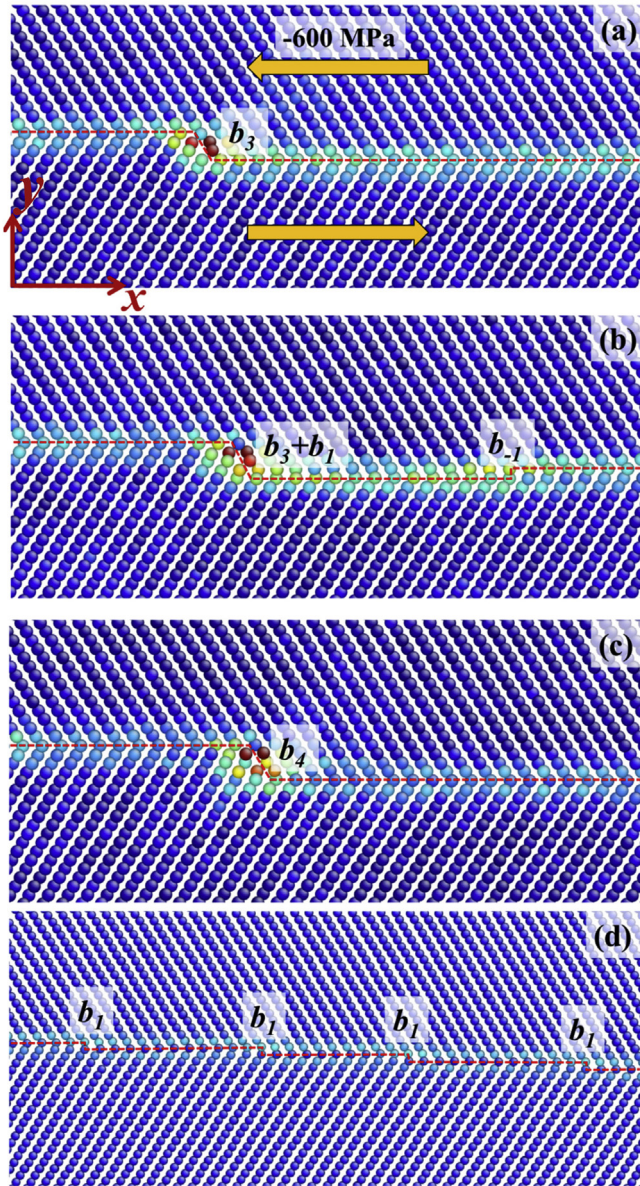
Fig. 7. Steps reassembly associated with the glide of one (b_3, $3h_{\{11\bar{2}2\}}$) TD under a shear stress of −600 MPa. (a) Initial three-layer step; (b) Nucleation of (b_1, $h_{\{11\bar{2}2\}}$) TD loop and glide of (b_{-1}, $-h_{\{11\bar{2}2\}}$) TD; (c) Formation of a four-layer step (b_4, $4h_{\{11\bar{2}2\}}$) TD. (d) Atomic structure of four (b_1, $h_{\{11\bar{2}2\}}$) TDs. The x-axis is along $[\bar{1}1\bar{2}3]$ direction, the y-axis is normal to ($11\bar{2}2$) plane and the z-axis is along $[\bar{1}100]$ direction.

basal $<a>$ dislocation (Fig. 8a) with the Burgers vector $(0.158, -0.250, 0)$ nm in the upper grain by applying the aniso-tropic Barnett-Lothe solutions [47] for the displacement field of a dislocation in the bi-crystal. During simulation, periodic boundary conditions are applied in the z-direction. Fixed boundary conditions are applied in the x- and y-directions to maintain the displacement field associated with $<a>$ dislocation.

Possible reactions corresponding to interactions between single edge basal $<a>$ dislocation and ($11\bar{2}2$) twin are summarized in Supplementary Table S-4. Generation of lattice dislocations is ruled out since the reactions increase total elastic energy. Under an applied deformation gradient $\mathbf{F_1}$ which generates resolved shear stress of 0.90 GPa on the basal plane in the upper grain, shear stress −1.23 GPa on the twin boundary (which favors ($11\bar{2}2$)

twinning), shear stress 0.61 GPa on ($\bar{1}\bar{1}21$) plane and −1.00 GPa on ($\bar{1}012$) plane in the lower grain.

$$\mathbf{F}_1 = \begin{pmatrix} 0.9941 & -0.02 & 0 \\ 0 & 0.9864 & 0 \\ 0 & 0 & 1 \end{pmatrix} \quad (5)$$

Fig. 8b shows one snapshot, demonstrating the nucleation and glide of one (b_1, $h_{\{11\bar{2}2\}}$) TD at the interaction site when the leading partial dislocation interacts with the CTB. The reaction can be written as $\frac{1}{3}[01\bar{1}0]_M \rightarrow b_1 + b_M^{r'}$. The dissociation is caused by the relatively lower core energy of (b_1, $h_{\{11\bar{2}2\}}$) TD. Secondary twinning doesn't happen because of low/negative shear stress.

To evoke nucleation of $\{11\bar{2}1\}$ twin, we change the applied deformation gradient to enhance shear stress on ($\bar{1}\bar{1}21$) plane in the lower grain while to suppress the glide of (b_1, $h_{\{11\bar{2}2\}}$) TD on the CTB. We tested two deformation gradients $\mathbf{F_2}$ and $\mathbf{F_3}$.

$$\mathbf{F}_2 = \begin{pmatrix} 1.01 & 0 & 0 \\ 0 & 0.9925 & 0 \\ 0 & 0 & 1 \end{pmatrix} \quad (6)$$

which generates resolved shear stress 0.91 GPa on the basal plane in the upper grain, shear stress 0 GPa on the CTB (which prevents nucleation and gliding of twinning dislocations on the CTB), and shear stress 1.00 GPa on ($\bar{1}\bar{1}21$) plane and −0.34 GPa on ($\bar{1}012$) plane in the lower grain.

$$\mathbf{F}_3 = \begin{pmatrix} 1.0259 & 0.02 & 0 \\ 0 & 0.9988 & 0 \\ 0 & 0 & 1 \end{pmatrix} \quad (7)$$

Which generates resolved shear stress 0.92 GPa on the basal plane in the upper grain, shear stress 1.23 GPa on the CTB (which favors ($11\bar{2}2$) detwinning), and shear stress 1.37 GPa on ($\bar{1}\bar{1}21$) plane and 0.32 GPa on ($\bar{1}012$) plane in the lower grain.

MD simulations revealed similar results for the two applied deformation gradients. Fig. 8c and d show two snapshots, revealing nucleation and growth of one ($\bar{1}\bar{1}21$) secondary twin inside the primary ($11\bar{2}2$) twin induced by larger shear stress on ($\bar{1}\bar{1}21$) plane. The reaction is described by $\frac{1}{3}[\bar{1}\bar{1}20]_M \rightarrow 6b_t^{(\bar{1}121)} + b_M^{r''}$. The result seems consistent with the EBSD observation [2].

4.2. Basal <a> dislocation interactions with a 3D $\left\{11\bar{2}2\right\}$ twin

Recently, we conducted 3D atomistic simulation of the inter-action processes of basal $<a>$ dislocations approaching a three-dimensional (3D) $\{\bar{1}012\}$ twin in Mg, and found that 3D atom-istic simulation complements the geometric/crystallographic analysis [54–58] and provides a comprehensive understanding of dislocation-twin interactions. Here we expect that 3D atomistic simulation may exhibit some additional information other than the 2D simulation.

We firstly created one ($11\bar{2}2$) twin domain in a $40 \times 40 \times 40$ nm single crystal. The single crystal adopts the coordinates where x-axis is along $[\bar{1}1\bar{2}3]$ direction, the y-axis is normal to ($11\bar{2}2$) plane and the z-axis is along $[\bar{1}100]$ direction. The ($11\bar{2}2$) twin is infinite long in x-direction (or the twinning shear direction). Periodic boundary condition is applied in the z-direction and fixed bound-ary conditions are in the x- and y-directions. Observed along the twinning shear direction, the twin has a hexagonal shape (Fig. 9a) that is outlined by two CTBs and four $\{1\bar{2}11\} \parallel \{\bar{1}2\bar{1}1\}$ interfaces
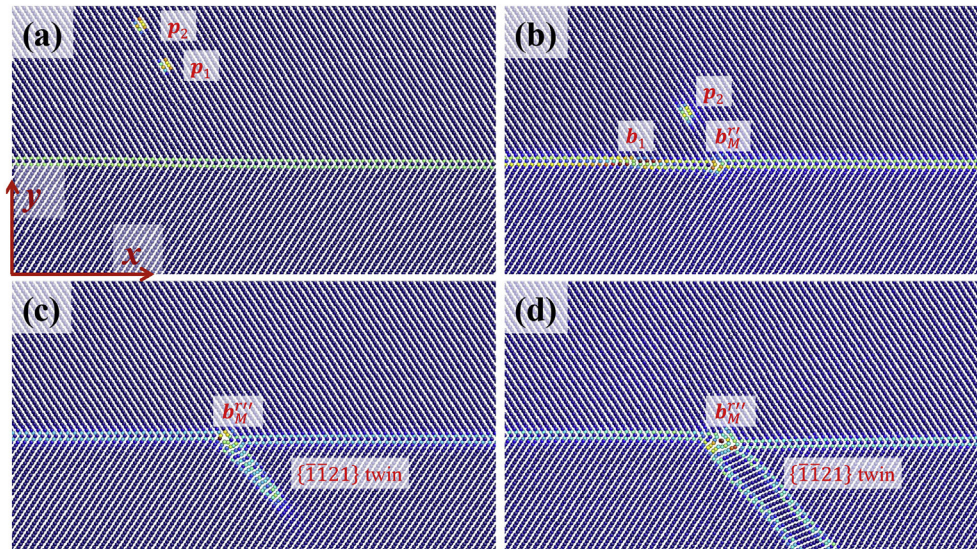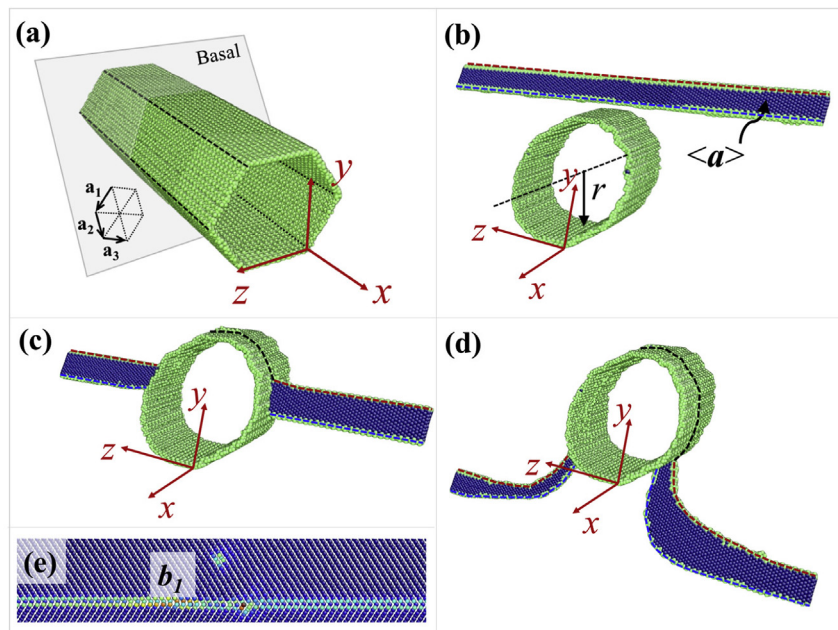
Fig. 8. Basal <***a***> dislocation interactions with a 2D {11$\bar{2}$2} twin. (a) Initial structure containing a coherent twin boundary and a pure edge basal <***a***> dislocation. (b) The formation of one-layer TD under the applied deformation gradient **F$_1$**. (c) and (d) The formation of a ($\bar{1}\bar{1}$21) secondary twin after slip transformation under applied deformation gradients **F$_2$** and **F$_3$**. The x-axis is along [$\bar{1}\bar{1}$23] direction, the y-axis is normal to (11$\bar{2}$2) plane and the z-axis is along [$\bar{1}$100] direction.

Fig. 9. Basal <***a***> dislocations interactions with a 3D {11$\bar{2}$2} twin under the applied deformation gradient **F$_1$**. (a) Initial structure of a 3D (11$\bar{2}$2) twin domain. (b) Relaxed structure of the 3D (11$\bar{2}$2) twin and a pure edge basal <***a***> dislocation. Blue dashed line represents the leading partial dislocation and red dashed line represents the trailing partial dislocation. (c) The dislocation is blocked by the twin and then loops the twin. (d) The dislocation nearly passes the twin domain by looping it. (e) A close look at the cross-section of the twin-dislocation intersection on the [$\bar{1}$100] direction, showing the formation of one-layer TD. Which is consistent with Fig. 11b. (For interpretation of the references to color in this figure legend, the reader is referred to the Web version of this article.)

because of their low interface energies (285 mJ/m^2 for CTB and 265 mJ/m^2 for {1$\bar{2}$11} ∥ {$\bar{1}$2$\bar{1}$1} interface). We introduced a pure edge <***a***> dislocation on basal plane by the application of the anisotropic Barnett-Lothe solutions [47] for the displacement field of a dislocation. The model containing the dislocation and a twin was relaxed for 5 pico-seconds at 10 K. Fig. 9b shows the relaxed structure where the (11$\bar{2}$2) twin is in a cylinder shape with the radius *r* of about 5 nm. The basal dislocation has a planar extended core. Similar to the 2D simulation, we applied deformation gradients **F$_1$**, **F$_2$** and **F$_3$**, respectively.

Under the deformation gradient **F$_1$**, the dislocation approaches the twin (also see Supplementary movie S-5). Fig. 9c and d show the looping processes of the dislocation around the twin. When we took a close look at the cross-section of the twin along the z-direction, one (***b$_1$***, $h_{\{11\bar{2}2\}}$) TD was observed on the CTB, as shown in Fig. 9e, which is consistent with the 2D simulation.

Under the deformation gradients **F$_2$** or **F$_3$**, the dislocation loops the twin and finally passes the twin, as shown in Fig. 10a. Interestingly, {11$\bar{2}$1} secondary twin nucleated inside the primary twin
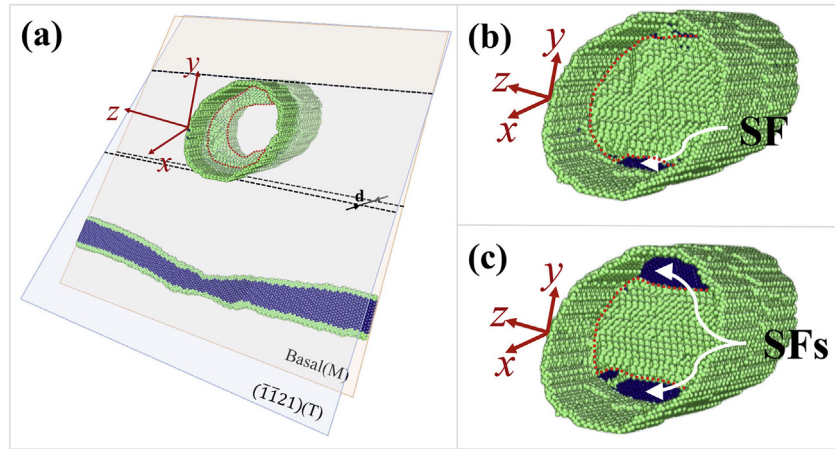
Fig. 10. Basal <*a*> dislocations interactions with a 3D {11$\bar{2}$2} twin under the applied deformation gradients **F**$_2$ or **F**$_3$. (a) Nucleation of ($\bar{1}\bar{1}$21) secondary twin at TBs of (11$\bar{2}$2) twin after the dislocation loops the twin. (b) Coalescence of secondary twins and the formation of basal stacking faults at the lower TB. (c) Formation of one secondary twin and basal stacking faults.
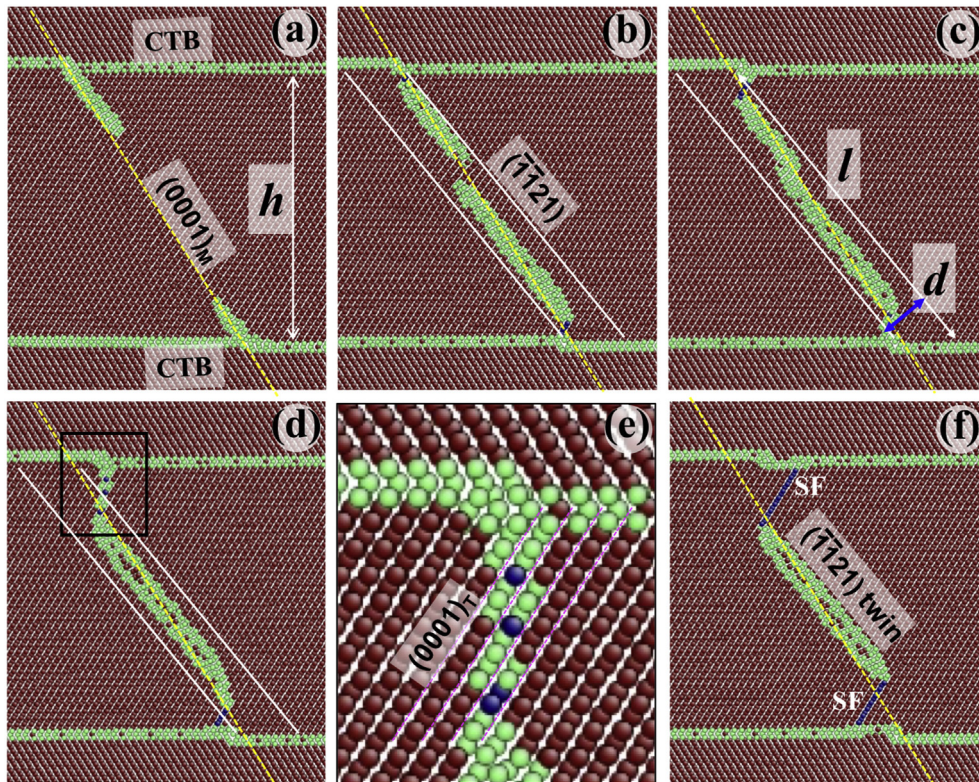

Fig. 11. 2D views of basal <*a*> dislocations interactions with a 3D {11$\bar{2}$2} twin under the applied deformation gradients **F**$_2$ or **F**$_3$. (a) Nucleation of secondary twins ($\bar{1}\bar{1}$21) at the upper and lower TBs. (b) Propagation/growth of ($\bar{1}\bar{1}$21) twins. The dashed yellow line is parallel to basal plane in matrix and two solid white lines are parallel to ($\bar{1}\bar{1}$21) plane in (11$\bar{2}$2) twin. (c) ($\bar{1}\bar{1}$21) twins meet and coalesce. (d) and (f) The evolution processes of ($\bar{1}\bar{1}$21) twins, accompanying the successive emission of basal <*a*> dislocations on basal plane in the primary twin, as shown in (e). Pink dashed lines in (e) show the gliding planes. (For interpretation of the references to color in this figure legend, the reader is referred to the Web version of this article.)

(Fig. 10c, also see Supplementary movie S-6). The primary $\{11\bar{2}2\}$ and the $\{11\bar{2}1\}$ secondary twin share the same zone axis. In order to clearly exhibit the formation processes of the $\{11\bar{2}1\}$ twin, we show 3D and 2D cross-sectional views. In 3D view, Fig. 10a shows atomic structure after the dislocation loops pass the twin. A loop-like shear region was observed near the twin boundary inside the

primary twin (Fig. 10a); then it propagates and coalesces in the primary twin, forming a shear band inside the primary twin (Fig. 10b); the shear band further develops into a $\{11\bar{2}1\}$ twin which connects with the lateral boundaries of the primary twin (Fig. 10c). Besides, basal stacking faults form and connect the $\{11\bar{2}1\}$ twin with twin boundaries of the primary twin. The cross-sectional views of the model in the z-plane clearly exhibit the initial nucleation and coalescence of a loop-like shear band and the

formation of the $\{11\bar{2}1\}$ secondary twin. Fig. 11a shows two shear regions that are connected to the upper and lower coherent twin boundaries after the dislocation loops the twin (also see Supplementary movie S-7). The yellow line indicates the basal plane in the matrix, demonstrating that the two shear regions are evoked by the dislocation-twin interaction. Fig. 11b and c show the propagation and coalescence of the two shear regions inside the primary twin. The two white lines indicate $(\bar{1}\bar{1}21)$ planes in the primary twin, implying the shear happens on $(\bar{1}\bar{1}21)$ planes. Fig. 11d and f show that the two shear regions further develop a single twin band accompanying complicated reassembly of defects at/near the twin boundary (zoomed in Fig. 11e) and formation of basal stacking faults. Fig. 11f shows a lenticular shape $(\bar{1}\bar{1}21)$ twin and two basal stacking faults inside the primary twin. Obviously, the $(\bar{1}\bar{1}21)$ twin does not connect to the dislocation-TB interaction sites, which is different from 2D simulations.

The above processes are attributed to two facts. First, twin bands are evoked by the dislocation-TB interaction. These initial twins nucleate on the different $(\bar{1}\bar{1}21)$ planes because the basal plane in the matrix is not parallel to the $(\bar{1}\bar{1}21)$ plane in the twin. Second, these twins on different planes develop a single twin band by reducing the energy associated with multiple twins. When the loop-like twins meet inside the primary twin, an irregular-shape $(\bar{1}\bar{1}21)$ twin forms. Given the projection of the height of $(\bar{1}\bar{1}21)$ twin on the normal of CTB is h, the angle between the yellow line and CTB is φ and the angle between the yellow line and the white line is θ, the thickness d of the irregular-shape $(\bar{1}\bar{1}21)$ twin is calculated to be $d = \frac{h}{\sin \varphi} \sin \theta$ and the length is $l = \frac{h}{\cos(\varphi - \theta)}$. h is 10.3 nm, φ is $57.8°$ and θ is $8.0°$. Therefore, the twin length is $l = 16.0$ nm and the thickness is $d = 1.70$ nm. After the twin develops a single twin band, the twin becomes shorter and thinner, $l = 7.4$ nm and $d = 0.8$ nm. Thus, reducing twin volume and twin boundaries enables the complicated reassembly of multiple twins and the emission of basal $<a>$ dislocations from the tips of the $\{11\bar{2}1\}$ twin.

5. Conclusion

We studied structures and energies of TDs, steps along coherent twin boundary and dislocation-twin interactions by combining microscopies and atomistic simulations. High-resolution transmission electron microscopies confirm the presence of various heights of steps along $\{11\bar{2}2\}$ twin boundary. Interestingly, the total height of a group of steps is equal to $3nh_{\{11\bar{2}2\}}$ $(n \geq 1)$. Atomistic simulations of twinning disconnections in terms of their energies and kinetics suggest that $(\boldsymbol{b_3}, 3h_{\{11\bar{2}2\}})$ TD is the elementary TD and $(\boldsymbol{b_1}, h_{\{11\bar{2}2\}})$ TD is the reassembly TD. Various height steps (or other TDs) can be treated as a reassembly TD of $(\boldsymbol{b_3}, 3h_{\{11\bar{2}2\}})$ TDs and $(\boldsymbol{b_1}, h_{\{11\bar{2}2\}})$ TD. In addition, two-dimensional and three-dimensional MD simulations of the interactions between basal $<a>$ dislocation and $\{11\bar{2}2\}$ twin demonstrated that $(\boldsymbol{b_1}, h_{\{11\bar{2}2\}})$ TD and $\{11\bar{2}2\} \rightarrow \{11\bar{2}1\}$ double twin can be nucleated depending on applied stresses. Our results extend our understanding of $\{11\bar{2}2\}$ twinning and $\{11\bar{2}2\} \rightarrow \{11\bar{2}1\}$ double twinning in hexagonal metals.

Acknowledgments

Appendix A. Supplementary data

Supplementary data to this article can be found online at https://doi.org/10.1016/j.actamat.2018.11.019.

References

[1] J.W. Christian, S. Mahajan, Deformation twinning, Prog. Mater. Sci. 39 (1995) 1—157.

[2] S. Xu, M. Gong, Y. Jiang, C. Schuman, J.-S. Lecomte, J. Wang, Secondary twin variant selection in four types of double twins in titanium, Acta Mater. 152 (2018) 58—76.

[3] T. Bieler, P. Eisenlohr, C. Zhang, H. Phukan, M. Crimp, Grain boundaries and interfaces in slip transfer, Curr. Opin. Solid State Mater. Sci. 18 (2014) 212—226.

[4] L. Wang, P. Eisenlohr, Y. Yang, T. Bieler, M. Crimp, Nucleation of paired twins at grain boundaries in titanium, Scripta Mater. 63 (2010) 827—830.

[5] A.A. Salem, S.R. Kalidindi, R.D. Doherty, Strain hardening of titanium: role of deformation twinning, Acta Mater. 51 (2003) 4225—4237.

[6] P. Zhou, D. Xiao, C. Jiang, G. Sang, D. Zou, Twin interactions in pure Ti under high strain rate compression, Metall. Mater. Trans. 48 (2017) 126—138.

[7] F. Xu, X. Zhang, H. Ni, Q. Liu, {11-24} deformation twinning in pure Ti during dynamic plastic deformation, Mater. Sci. Eng., A 541 (2012) 190—195.

[8] N.E. Paton, W. Backofen, Plastic deformation of titanium at elevated temperatures, Metall. Trans. 1 (1970) 2839—2847.

[9] N.P. Gurao, R. Kapoor, S. Suwas, Deformation behaviour of commercially pure titanium at extreme strain rates, Acta Mater. 59 (2011) 3431—3446.

[10] H. Qin, J.J. Jonas, Variant selection during secondary and tertiary twinning in pure titanium, Acta Mater. 75 (2014) 198—211.

[11] S. Mullins, B. Patchett, Deformation microstructures in titanium sheet metal, Metall. Trans. A 12 (1981) 853—863.

[12] S. Bouvier, N. Benmhenni, W. Tirry, F. Gregory, M. Nixon, O. Cazacu, L. Rabet, Hardening in relation with microstructure evolution of high purity α-titanium deformed under monotonic and cyclic simple shear loadings at room temperature, Mater. Sci. Eng., A 535 (2012) 12—21.

[13] B.M. Morrow, R.J. McCabe, E.K. Cerreta, C.N. Tomé, Observations of the atomic structure of tensile and compressive twin boundaries and twin—twin interactions in zirconium, Metall. Mater. Trans. 45 (2014) 5891—5897.

[14] J. Bingert, T. Mason, G.C. Kaschner, G. Gray, P. Maudlin, Deformation twinning in polycrystalline Zr: insights from electron backscattered diffraction characterization, Metall. Mater. Trans. 33 (2002) 955—963.

[15] Y. Guo, H. Abdolvand, T. Britton, A. Wilkinson, Growth of {112 2} twins in titanium: a combined experimental and modelling investigation of the local state of deformation, Acta Mater. 126 (2017) 221—235.

[16] T. Mason, J. Bingert, G. Kaschner, S. Wright, R. Larsen, Advances in deformation twin characterization using electron backscattered diffraction data, Metall. Mater. Trans. 33 (2002) 949—954.

[17] A. Berghezan, A. Fourdeux, S. Amelinckx, Transmission electron microscopy studies of dislocations and stacking faults in a hexagonal metal: Zinc, Acta Metall. 9 (1961) 464—490.

[18] G. Proust, C. Tomé, G. Kaschner, Modeling texture, twinning and hardening evolution during deformation of hexagonal materials, Acta Mater. 55 (2007) 2137—2148.

[19] Q. Yu, J. Wang, Y. Jiang, R.J. McCabe, C.N. Tomé, Co-zone {-1012} twin interaction in magnesium single crystal, Mater. Res. Lett. 2 (2014) 82—88.

[20] Q. Yu, Y. Jiang, J. Wang, Cyclic deformation and fatigue damage in single-crystal magnesium under fully reversed strain-controlled tension—compression in the [10-10] direction, Scripta Mater. 96 (2015) 41—44.

[21] Q. Yu, J. Zhang, Y. Jiang, Direct observation of twinning—detwinning—retwinning on magnesium single crystal subjected to strain-controlled cyclic tension—compression in [0 0 0 1] direction, Phil. Mag. Lett. 91 (2011) 757—765.

[22] J. Wang, S. Yadav, J. Hirth, C. Tomé, I. Beyerlein, Pure-shuffle nucleation of deformation twins in hexagonal-close-packed metals, Mater. Res. Lett. 1 (2013) 126—132.

[23] R.C. Pond, J. Hirth, A. Serra, D. Bacon, Atomic displacements accompanying deformation twinning: shears and shuffles, Mater. Res. Lett. 4 (2016) 185—190.

[24] B.-Y. Liu, J. Wang, B. Li, L. Lu, X.-Y. Zhang, Z.-W. Shan, J. Li, C.-L. Jia, J. Sun, E. Ma, Twinning-like lattice reorientation without a crystallographic twinning plane, Nat. Commun. 5 (2014).

[25] J.P. Hirth, J. Lothe, Theory of Dislocations, 1982.

[26] J. Wang, I.J. Beyerlein, J.P. Hirth, C.N. Tomé, Twinning dislocations on {1011} and {1013} planes in hexagonal close-packed crystals, Acta Mater. 59 (2011)

3990—4001.

[27] J. Wang, L. Liu, C.N. Tomé, S.X. Mao, S.K. Gong, Twinning and de-twinning via glide and climb of twinning dislocations along serrated coherent twin boundaries in hexagonal-close-packed metals, Mater. Res. Lett. 1 (2013) 81—88.

[28] F. Frank, LXXXIII. Crystal dislocations.—elementary concepts and definitions, the London, Edinburgh, and Dublin, Phil. Mag. J. Sci. 42 (1951) 809—819.

[29] R. Pond, J. Hirth, Defects at surfaces and interfaces, Solid State Phys. 47 (1994) 287—365.

[30] E. Rapperport, C.S. Hartley, Deformation Modes of Zirconium at 77 K, 300 K, 575 K, and 1075 K, Nuclear Metals, Inc., Concord, Mass., 1960.

[31] R. Pond, D. Bacon, A. Serra, A. Sutton, The crystallography and atomic structure of line defects in twin boundaries in hexagonal-close-packed metals, Metall. Trans. A 22 (1991) 1185—1196.

[32] A. Serra, D. Bacon, R. Pond, The crystallography and core structure of twinning dislocations in hcp metals, Acta Metall. 36 (1988) 3183—3203.

[33] A. Serra, D. Bacon, Modelling the motion of {11-22} twinning dislocations in the HCP metals, Mater. Sci. Eng., A 400—401 (2005) 496—498.

[34] H. El Kadiri, C.D. Barrett, J. Wang, C.N. Tomé, Why are twins profuse in magnesium? Acta Mater. 85 (2015) 354—361.

[35] A. Serra, D. Bacon, R. Pond, Twins as barriers to basal slip in hexagonal-close-packed metals, Metall. Mater. Trans. 33 (2002) 809—812.

[36] J. Wang, I. Beyerlein, C. Tomé, Reactions of lattice dislocations with grain boundaries in Mg: implications on the micro scale from atomic-scale calculations, Int. J. Plast. 56 (2014) 156—172.

[37] I.J. Beyerlein, J. Wang, M.R. Barnett, C.N. Tome, Double twinning mechanisms in magnesium alloys via dissociation of lattice dislocations, Proc. R Soc. A Math. 468 (2012) 1496—1520.

[38] S. Xu, M. Gong, C. Schuman, J.-S. Lecomte, X. Xie, J. Wang, Sequential {10-12} twinning stimulated by other twins in titanium, Acta Mater. 132 (2017) 57—68.

[39] K.D. Molodov, T. Al-Samman, D.A. Molodov, Profuse slip transmission across twin boundaries in magnesium, Acta Mater. 124 (2017) 397—409.

[40] A. Serra, D. Bacon, Computer simulation of screw dislocation interactions with twin boundaries in HCP metals, Acta Metall. 43 (1995) 4465—4481.

[41] F. Wang, S.R. Agnew, Dislocation transmutation by tension twinning in magnesium alloy AZ31, Int. J. Plast. 81 (2016) 63—86.

[42] L. Capolungo, I. Beyerlein, G. Kaschner, C. Tomé, On the interaction between slip dislocations and twins in HCP Zr, Mater. Sci. Eng., A 513 (2009) 42—51.

[43] A.A. Salem, S. Kalidindi, R. Doherty, S. Semiatin, Strain hardening due to deformation twinning in α-titanium: mechanisms, Metall. Mater. Trans. 37 (2006) 259—268.

[44] M. Gong, G. Liu, J. Wang, L. Capolungo, C.N. Tomé, Atomistic simulations of interaction between basal< a> dislocations and three-dimensional twins in Magnesium, Acta Mater. 155 (2018) 187—198.

[45] J. Hirth, J. Wang, C. Tomé, Disconnections and other defects associated with twin interfaces, Prog. Mater. Sci. 83 (2016) 417—471.

[46] R.R. Zope, Y. Mishin, Interatomic potentials for atomistic simulations of the Ti-Al system, Phys. Rev. B 68 (2003) 024102.

[47] D. Barnett, J. Lothe, An image force theorem for dislocations in anisotropic bicrystals, J. Phys. F Met. Phys. 4 (1974) 1618.

[48] G. Henkelman, H. Jónsson, Improved tangent estimate in the nudged elastic band method for finding minimum energy paths and saddle points, J. Chem. Phys. 113 (2000) 9978—9985.

[49] M.H. Yoo, C.T. Wei, Slip modes of hexagonal-close-packed metals, J. Appl. Phys. 38 (1967) 4317—4322.

[50] I. Shin, E.A. Carter, Simulations of dislocation mobility in magnesium from first principles, Int. J. Plast. 60 (2014) 58—70.

[51] S. Groh, E.B. Marin, M.F. Horstemeyer, D.J. Bammann, Dislocation motion in magnesium: a study by molecular statics and molecular dynamics, Model. Simulat. Mater. Sci. Eng. 17 (2009) 075009.

[52] R. Lebensohn, C. Tomé, A study of the stress state associated with twin nucleation and propagation in anisotropic materials, Philos. Mag. A 67 (1993) 187—206.

[53] J. Wang, I.J. Beyerlein, C.N. Tomé, Reactions of lattice dislocations with grain boundaries in Mg: implications on the micro scale from atomic-scale calculations, Int. J. Plast. 56 (2014) 156—172.

[54] A.W. Sleeswyk, C.A. Verbraak, Incorporation of slip dislocations in mechanical twins—I, Acta Metall. 9 (1961) 917—927.

[55] M.H. Yoo, Interaction of slip dislocations with twins in hcp metals, Trans. Metall. Soc. AIME 245 (1969), 2061-2060.

[56] I. Saxl, The incorporation of slip dislocations in twins, Czech. J. Phys. 18 (1968) 39—49.

[57] M.H. Yoo, C.T. Wei, Growth of deformation twins in zinc crystals, Phil. Mag. 14 (1966) 573—587.

[58] M. Niewczas, Lattice correspondence during twinning in hexagonal close-packed crystals, Acta Mater. 58 (2010) 5848—5857.

Steps and {11$\bar{2}$1} secondary twinning associated with {11$\bar{2}$2} twin in titanium

Mingyu Gong [a,Δ], Shun Xu [a,Δ], Dongyue Xie [a], Shujuan Wang [b], Jian Wang [a,c,*],

Christophe Schuman [d], Jean-Sébastien Lecomte [d]

[a] Mechanical and Materials Engineering, University of Nebraska-Lincoln, Lincoln, NE 68588, USA

[b] MST-8, Los Alamos National Laboratory, Los Alamos, NM 87545, USA

[c] Nebraska Center for Materials and Nanoscience, University of Nebraska-Lincoln, Lincoln, NE 68588, USA

[d] Laboratoire d'Etude des Microstructures et de Mecanique des Materiaux (LEM3), CNRS UMR 7239; Laboratory of Excellence on Design of Alloy Metals for low-mAss Structures (DAMAS), Universite de Lorraine, F-57045, Metz, France

S-1 Comparison of properties from MD, DFT and experimental measurements.

	a (Å)	c (Å)	E_{coh} (eV)	C_{11} (GPa)	C_{33} (GPa)	C_{12} (GPa)	C_{13} (GPa)	C_{44} (GPa)	γ_{sf} (eV)
EAM	2.95	4.68	-4.85	171	190	84	77	52	56
GGA	2.95[a]	4.68[a]	-5.17[b]	172[a]	190[a]	82[a]	75[a]	45[a]	292[a]
Exp.	2.95[c]	4.69[c]	-4.85[d]	176[e]	190[e]	87[e]	68[e]	51[e]	290[f]

a. DR Trinkle, MD Jones, RG Hennig, SP Rudin, RC Albers, JW Wilkins. Empirical tight-binding model for titanium phase transformations. *Physical Review B*, *73*.9 (2006), p.094123.

b. RG Hennig, TJ Lenosky, DR Trinkle, SP Rudin, JW Wilkins. Classical potential describes martensitic phase transformations between the α, β, and ω titanium phases. *Physical Review B*, *78*.5 (2008), p.054121.

c. WB Pearson. A handbook of lattice spacing and structure of metals and alloys (Pergamon, Oxford, 1987). Vol. 1-2.

d. C Kittel, P McEuen. Introduction to solid state physics (New York: Willey, 1996). Vol. 8, p. 323-324.

e. G Simons, H Wang. Single crystal elastic constants and calculated aggregate properties (MIT, Cambridge, MA, 1977).

f. PB Legrand. Relations entre la structure électronique et la facilité de glissement dans les métaux hexagonaux compacts. *Philosophical Magazine B*, *49*(2) (1984), pp.171-184.

Properties including lattice constants, cohesive energy and elastic modulus from Zope and Mishin's EAM potential have good agreement with DFT results and experimental measurements. The stacking fault energy on basal plane from MD simulation is lower than that from DFT or experiments. This will cause a slightly increased separation between two partial dislocations on basal plane, but no significant influence on the interaction process between edge basal <**a**> dislocation and {11$\bar{2}$2} twin.

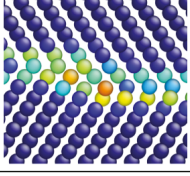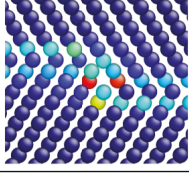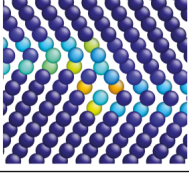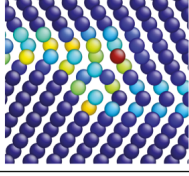[Δ] Mr. MY Gong and Dr. S Xu contributed equally to this work.
[*] Corresponding authors: Dr. Jian Wang (jianwang@unl.edu)
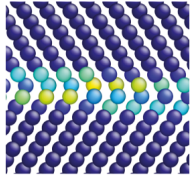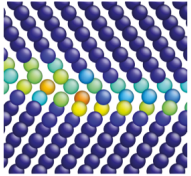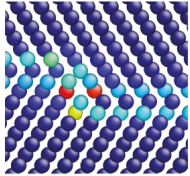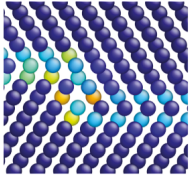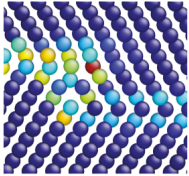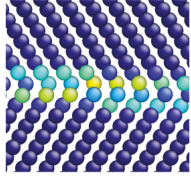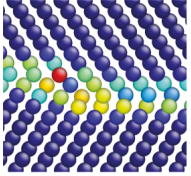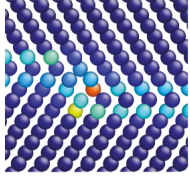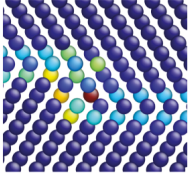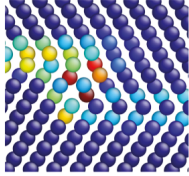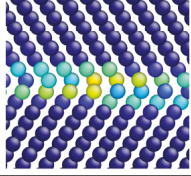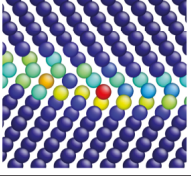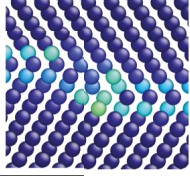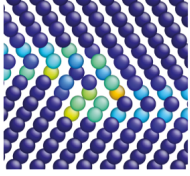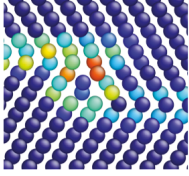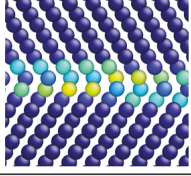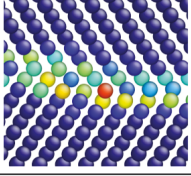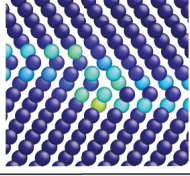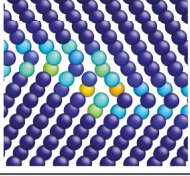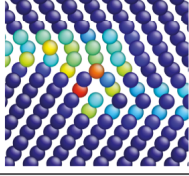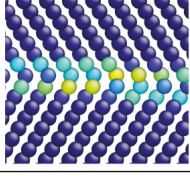
S-2 Atoms movements associated with glide of (a) (b_1, $h_{\{11\bar{2}2\}}$) TD, (b) (b_3, $3h_{\{11\bar{2}2\}}$) TD and (c) (b_4, $4h_{\{11\bar{2}2\}}$) TD in MD simulations. (At finite temperature, (b_2, $2h_{\{11\bar{2}2\}}$) TD will dissociate into (b_3, $3h_{\{11\bar{2}2\}}$) TD and (b_{-1}, $-1h_{\{11\bar{2}2\}}$) TD. Meanwhile, (b_5, $5h_{\{11\bar{2}2\}}$) TD will dissociate into (b_4, $4h_{\{11\bar{2}2\}}$) TD and (b_1, $h_{\{11\bar{2}2\}}$) TD.) Red arrows have around 0.085 nm displacement in z-direction, blue arrows have around -0.085 nm displacement in z-direction and black arrows have around 0 nm displacement in z-direction. The MD results are comparable to the TM analysis.
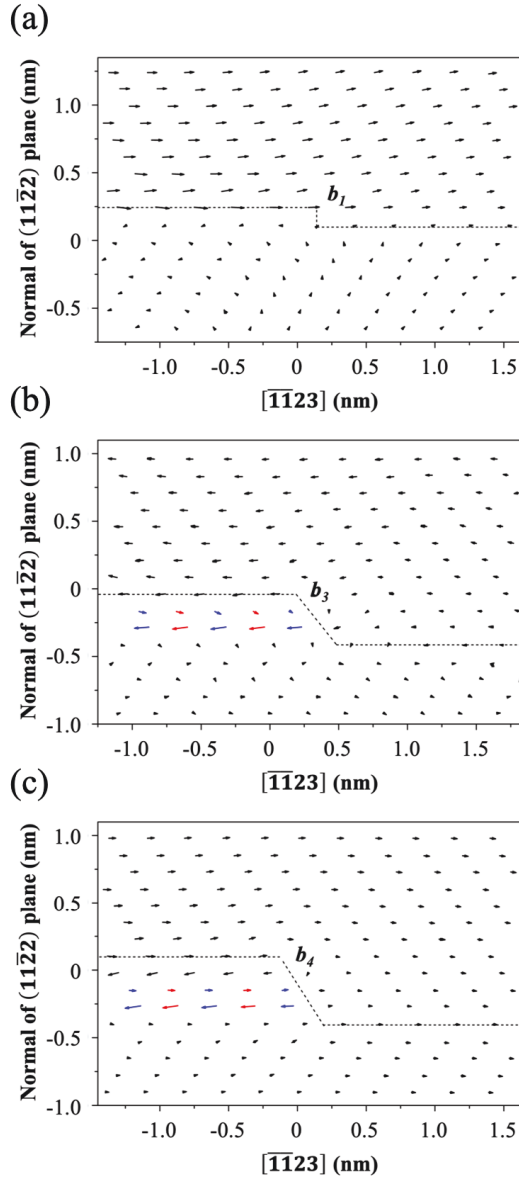
(a)

(b)

(c)

Atoms movements associated with glide of (a) (b_1, $h_{\{11\bar{2}2\}}$) TD, (b) (b_3, $3h_{\{11\bar{2}2\}}$) TD and (c) (b_4, $4h_{\{11\bar{2}2\}}$) TD in MD simulations.

S-3 Minimum energy path associated with glide of $(b_1, h_{\{11\bar{2}2\}})$ TD, $(b_2, 2h_{\{11\bar{2}2\}})$ TD, $(b_3, 3h_{\{11\bar{2}2\}})$ TD, $(b_4, 4h_{\{11\bar{2}2\}})$ TD and $(b_5, 5h_{\{11\bar{2}2\}})$ TD.

S-4 Possible reactions during interaction between single pure edge basal <**a**> dislocation and $(11\bar{2}2)$ CTB.

Possible reaction	$\dfrac{\Sigma\lvert b_{right}\rvert^2 - \Sigma\lvert b_{left}\rvert^2}{\lvert a\rvert^2}$	SS (GPa) of product (F_1, F_2, F_3)
1. Pure edge basal <**a**> in twin $\frac{1}{3}[\bar{1}\bar{1}20]_M \rightarrow \frac{1}{3}[11\bar{2}0]_T + \boldsymbol{b^{r_1}}$	1.14	0.16, -0.91, -1.97
2. Mixed basal <**a**> in twin $\frac{1}{3}[\bar{1}\bar{1}20]_M \rightarrow \frac{1}{3}[\bar{1}2\bar{1}0]_T / \frac{1}{3}[2\bar{1}\bar{1}0]_T + \boldsymbol{b^{r_2}}/\boldsymbol{b^{r_3}}$	1.57	0.08, -0.46, -0.99
3. Pure edge prismatic <**a**> in twin $\frac{1}{3}[\bar{1}\bar{1}20]_M \rightarrow \frac{1}{3}[11\bar{2}0]_T + \boldsymbol{b^{r_1}}$	1.14	0, 0, 0
4. Mixed prismatic <**a**> in twin $\frac{1}{3}[\bar{1}\bar{1}20]_M \rightarrow \frac{1}{3}[\bar{1}2\bar{1}0]_T / \frac{1}{3}[2\bar{1}\bar{1}0]_T + \boldsymbol{b^{r_2}}/\boldsymbol{b^{r_3}}$	1.57	1.04, 0.09, -0.87
5. Pure edge 2nd pyramidal <**c+a**> in twin $\frac{1}{3}[\bar{1}\bar{1}20]_M \rightarrow \frac{1}{3}[11\bar{2}3]_T + \boldsymbol{b^{r_4}}$	3.30	1.10, 0.79, 0.48
6. TDs of $\{\bar{1}012\}$ twinning in twin $\frac{1}{3}[\bar{1}\bar{1}20]_M \rightarrow 4b_t^{(10\bar{1}2)} + \boldsymbol{b^{r_5}}$	-0.61	-1.00, -0.34, 0.32
7. TDs of $\{11\bar{2}1\}$ twinning in twin $\frac{1}{3}[\bar{1}\bar{1}20]_M \rightarrow 6b_t^{(\bar{1}\bar{1}21)} + \boldsymbol{b^{r_6}}$	-0.84	0.61, 1.00, 1.37
8. $\boldsymbol{b_1}$ TDs of $\{11\bar{2}2\}$ twinning in matrix $\frac{1}{3}[\bar{1}\bar{1}20]_M \rightarrow \boldsymbol{b_1} + \boldsymbol{b^{r_7}}$	0.00	-1.23, 0, 1.23
9. $\boldsymbol{b_3}$ TDs of $\{11\bar{2}2\}$ twinning in matrix $\frac{1}{3}[\bar{1}\bar{1}20]_M \rightarrow -\boldsymbol{b_3} + \boldsymbol{b^{r_8}}$	-0.14	1.23, 0, -1.23

In the above table, reactions 1-5 generate lattice dislocations. There's no requirement for the direction of shear stress (SS). So, shear stresses in table are displayed in positive value. Reactions 6 and 7 show nucleation of secondary twins which is directional. Only positive values of shear stress favor the reaction. Reactions 8 and 9 are the twinning/detwinning process of the primary twin. Positive value of shear stress indicates twinning and vice versa.

S-5 A movie showing 3D view of interaction processes between edge basal <*a*> dislocation and $\{11\bar{2}2\}$ twin under deformation gradient F_1. Atoms are displayed with respect to potential energy.
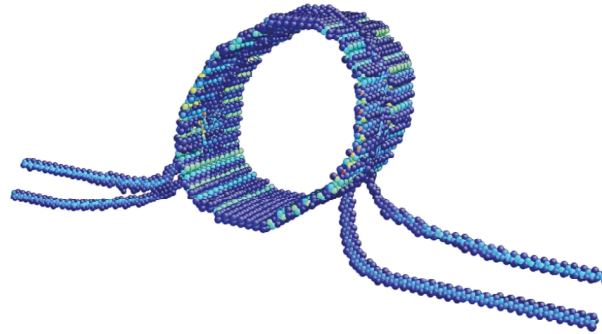
S-6 A movie showing 3D view of interaction processes between edge basal <*a*> dislocation and $\{11\bar{2}2\}$ twin under deformation gradient F_2 or F_2. Atoms are displayed with respect to common neighbor analysis (CNA). Blue color shows the I_2 stacking faults.
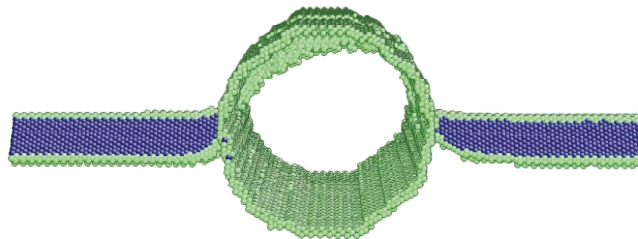
S-7 A movie showing 2D view of interaction processes between edge basal <*a*> dislocation and $\{11\bar{2}2\}$ twin under deformation gradient F_2 or F_2. Atoms are displayed with respect to common neighbor analysis (CNA). Blue color shows the I_2 stacking faults.